ACS OMEGA

Open Access

http://pubs.acs.org/journal/acsodf

Article

Synthesis of Lead(II) Carbonate-Containing Nanoparticles Using Ultrasonication or Microwave Irradiation

Madhushika E. Gamage, Kyan D. Ho, Mohammad S. Kader, Katherine Nguyen, Mirudhula Velmurugan, Sara H. McBride-Gagyi, Steven W. Buckner,* and Paul A. Jelliss*

Cite This: *ACS Omega* 2024, 9, 48802−48809

Read Online

ACCESS | Metrics & More | Article Recommendations | Supporting Information

ABSTRACT: We report on the synthesis of lead(II) carbonate-containing nanoparticles using the polyol process under high-energy ultrasound or microwave irradiation as alternate energization methods. Five carbonate source precursors are used in the reaction, and the precipitation reactions generate four different crystal products, depending on the precursor. More alkaline precursors produce the hydroxy-carbonate structures (abellaite, or its potassium analog, and hydrocerussite), while the less alkaline precursors produce the simple carbonate structure (cerussite). Ultrasonication or microwave irradiation during the arrested precipitation ensures the formation of nanoparticles <100 nm in diameter in a mostly single crystalline phase in all cases, bar one. The products were characterized by powder X-ray diffraction, dynamic light scattering, electron microscopy, infrared spectroscopy, and thermal analysis. These nanoparticles are targeted as X-ray contrast agents for biological imaging, particularly of fine vasculature where small particle size is essential.

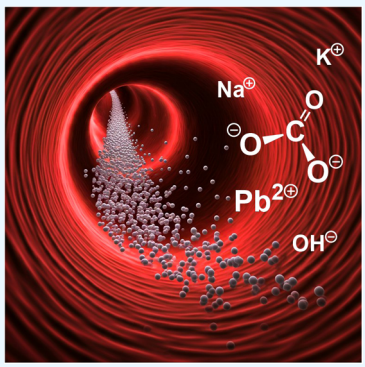

1. INTRODUCTION

X-rays interact with matter primarily via absorption and Compton scattering with absorption by core electrons the primary interaction pathway between period 6 elements and X-rays in the 50 kV to 1 MeV regime.[1] The period 6 elements have high X-ray absorption cross sections that make them favorable as components of X-ray contrast agents for biomedical imaging.[2−8] Often, salts of the main group period 6 elements, particularly those of barium and lead, are used due to their lower cost.[9−11] There are numerous examples of low solubility period 6 main group metal salt particles that have been applied as X-ray contrast agents, the most common being $BaSO_4$ used in gastrointestinal imaging. For finer imaging, nanoparticles are necessary to provide access to and resolution of fine biological structures such as vasculature.

Recently, we applied period 6 metal nanoparticles in alginate gels used for post-mortem fine vascular imaging with micro-CT.[12,13] One of the key factors in forming these gels is the release of divalent metal ions into solution to induce cross-linking of the alginate polymer. In order to release the metal ions it is necessary to have an acid-reactive salt. We used carbonate salts for this purpose. With decreasing pH, these salts release soluble divalent metal cations that result in gel formation.

Multiple methods for $PbCO_3$ nanoparticle synthesis have been reported.[14−18] The synthesis is generally performed via controlled precipitation reactions between Pb^{2+} and CO_3^{2-} containing salts as in eq 1.

$$PbX(aq) + M_2CO_3(aq) \rightarrow PbCO_3(s) + M_2X(aq) \quad (1)$$

However, $PbCO_3(s)$ has subtle chemistry that has not been fully recognized in the nanoscience community.[14−17] In this paper we present a study on synthesis of different lead(II) carbonate-containing structures as a function of reactant precursor. We discuss the ways these precursors affect the product outcomes for this seemingly simple precipitation reaction. In the process, we report on the preparation of three previously unreported nanoparticle structures. The NPs are acid-reactive and have excellent X-ray opacity, making them excellent candidates for micro-CT-based vascular imaging.

Our recent work has incorporated reaction mixture energization using an ultrasonic dismembrator to effectively mitigate particle growth beyond nanodimensional sizes during the precipitation process.[19] As an alternative, microwave irradiation has the advantage of providing immediate, uniform energy delivery throughout the reaction medium. As a direct result of their ability to penetrate and heat homogeneously, microwaves have been shown to both provide control over nanoparticle growth as well as to narrow size distributions. They have been used effectively to synthesize both metallic and metal salt nanoparticles.[20] The elevated temperature regime, whether thermal- or microwave-assisted, is also known to decrease nanoparticle size and size distribution by virtue of a

Received: September 26, 2024
Revised: November 15, 2024
Accepted: November 19, 2024
Published: November 26, 2024

kinetically expedited process.[21] In this work we explore the impact of microwave irradiation during precipitation in comparison to ultrasonication.

2. EXPERIMENTAL SECTION

2.1. Materials. $Pb(NO_3)_2$ (anhydrate, purity ≥99.0%), Na_2CO_3, K_2CO_3, $(NH_4)_2CO_3$, NH_4HCO_3, and $NaHCO_3$ were purchased from Millipore Sigma (St Louis, MO). Tetraethylene glycol (TEG; 99%, Alfa Aesar) was used as supplied.

2.2. Synthesis Equipment. The synthetic protocols for NPs were based on a polyol arrested precipitation reaction[22−25] between $Pb(NO_3)_2$ and soluble carbonate solutions in a mixture of TEG and water. High-intensity sonication using a sonic dismembrator (US Solids 1200 W Ultrasonic Homogenizer) pulsing 2 s on and 1 s off at a power of 900 W was applied during the nanoparticle formation. Microwave irradiation was carried out with a 1350 W, 2450 MHz FCMCR-3SX-T microwave reactor with a thermocouple temperature sensor, magnetic stirrer, and set to maintain the reaction mixture at 80 °C. The reactor setup is shown in Figure 1.

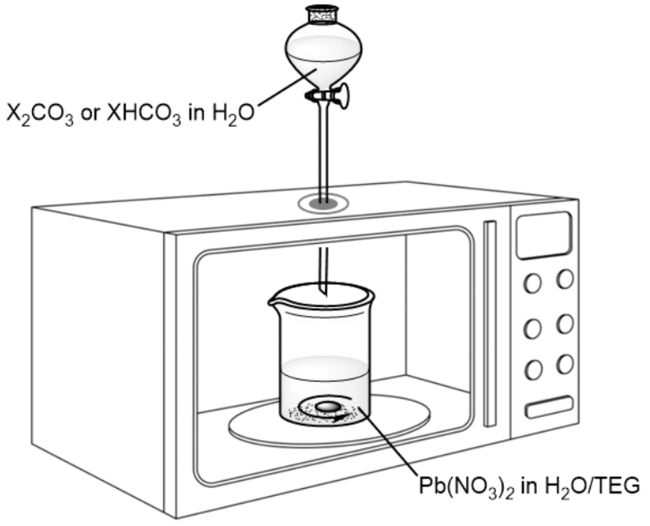

Figure 1. Microwave reactor setup for NPs synthesis. $X^+ = Na^+$, K^+, or NH_4^+.

2.3. Synthesis with Ultrasonication. A 1.45 *M* solution of $Pb(NO_3)_2$ in water was prepared by dissolving 12 g in 25 mL of DI water. The amounts and concentrations of the carbonate precursor solutions in water for the five reactions studied are shown in Table 1. The $Pb(NO_3)_2$ solution was combined with 100 mL of TEG in a plastic beaker using a glass rod to promote full dissolution of the TEG. To this mixture was added the appropriate carbonate precursor solution dropwise with a Pasteur pipet over the course of 10−15 min, while being subjected to high-intensity sonication using the sonic dismembrator. The final TEG concentration after combination was 62% (v/v) for the reactions using the carbonate precursors and 38 to 48% (v/v) for the reactions using bicarbonate precursors. The sonic dismembrator was tuned so that it was highly pitched, and the solution was visibly mixed throughout the addition. Drops of the corresponding carbonate precursor were added close to the sonic dismembrator probe at a rate of 2 drops/second. After the contents of the pipet were fully dispensed, the beaker was moved so that the probe reached the edges in a circular twisting motion and was then returned to the middle of the beaker. Once the addition was complete, a watch glass was placed on top of the beaker holding the suspended NPs for 5−6 h. Finally, the NP solution was centrifuged 4 times (3500 rpm, 15 min) and washed with DI water between each centrifugation, then dried in an oven at 110 °C for 10−12 h to yield the product powder.

2.4. Synthesis with Microwave Irradiation. A 1.45 *M* solution of $Pb(NO_3)_2$ in water was prepared by dissolving 12 g in 25 mL of DI water. The amounts and concentrations of the carbonate precursor solutions in water for the five reactions studied are shown in Table 1. The $Pb(NO_3)_2$ solution was combined with 100 mL of TEG in a glass beaker using a glass rod to promote full dissolution of the TEG. The beaker was placed in the microwave reactor and irradiated to a steady temperature of 80 °C. The appropriate carbonate precursor solution was added via a dropping funnel through the reactor access port over the course of 10−15 min with continuous stirring while irradiating. The final TEG concentration after combination was 62% (v/v) for the reactions using the carbonate precursors and 38 to 48% (v/v) for the reactions using bicarbonate precursors. Once the addition was complete, the flask was removed from the reactor and a watch glass was placed on top of the beaker holding the suspended NPs for 5−6 h. Finally, the NP solution was centrifuged 4 times (3500 rpm, 15 min) and washed with DI water between each centrifugation, then dried in an oven at 110 °C for 10−12 h to yield the product powder.

2.5. Characterization. Powder X-ray diffraction (PXRD) measurements were carried out with a Rigaku Miniflex 600 X-ray diffractometer with Cu Kα radiation (40 kV, 15 mA). Scanning was performed from 5 to 90° at a rate of 5°/min, with a step width of 0.02°. Crystalline phases were identified by comparison with the ICDD Crystallographic Database. The Scherrer equation was used to calculate the crystallite size of nanoparticles from the peak-width-at-half-height measurements of the three strongest reflections for any specific

Table 1. Parameters for the Carbonate-Containing Solutions

carbonate precursor	carbonate mass (g)	water volume (mL)	carbonate solution molarity (M)	solution pH	final TEG concentration (v/v)	yield (g)	
						US[a]	MW[b]
Na_2CO_3	5.72	20	2.7	12.38	62%	9.8	9.6
K_2CO_3	7.46	20	2.7	12.38	62%	9.1	8.6
$(NH_4)_2CO_3$	5.19	20	2.7	9.20	62%	8.6	8.6
$NaHCO_3$	9.06	96	1.1	8.34	38%	7.9	9.3
NH_4HCO_3	8.54	40	2.7	7.85	48%	7.6	9.2

[a]Ultrasonication method. [b]Microwave irradiation method.

https://doi.org/10.1021/acsomega.4c08839
ACS Omega 2024, 9, 48802−48809

Table 2. Identity and Average Crystallite Size Determined by PXRD of the TEG-Capped NP Diffracting Crystallites Produced Using the Different Carbonate Precursors and Using Either Ultrasonication or Microwave Irradiation[a,b]

		product distribution (wt %)		crystallite size (nm)[c]	
carbonate precursor	nanoparticle product identity	US[c]	MW[c]	US[c]	MW[c]
Na_2CO_3	$NaPb_2(CO_3)_2(OH)$ (ANPs)[d]	>99	>99	22 ± 1	21 ± 1
	$Pb_3(CO_3)_2(OH)_2$ (HCNPs)[e]	<1	<1	[f]	[f]
K_2CO_3	$KPb_2(CO_3)_2(OH)$ (KPbNPs)[g]	<5	60	[f]	21 ± 2
	$Pb_3(CO_3)_2(OH)_2$ (HCNPs)[e]	>95	40	25 ± 1	23 ± 1
$(NH_4)_2CO_3$	$PbCO_3$ (CNPs)[h]	100	100	19 ± 1	24 ± 1
$NaHCO_3$	$PbCO_3$ (CNPs)[h]	100	100	25 ± 2	20 ± 1
NH_4HCO_3	$PbCO_3$ (CNPs)[h]	100	100	19 ± 1	23 ± 1

[a]Determined from the average of measured Scherrer peak width-at-half-height for the strongest three reflections associated with any one phase. [b]Ultrasonication method. [c]Microwave irradiation method. [d]Abellaite nanoparticles. [e]Hydrocerussite nanoparticles. [f]Peaks too weak or obscured to be able to determine Scherrer peak widths. [g]Potassium analog of abellaite nanoparticles. [h]Cerussite nanoparticles.

phase. Product weight distributions for mixed-phase systems were determined using the WPPF/RIR method. Fourier transform infrared (FTIR) spectra were measured on powder samples using an Agilent Cary 630 ATR-FTIR spectrometer. Dynamic light scattering (DLS) measurements were recorded using a Zetasizer Ultra (Malvern Panalytical Ltd., UK), fitted with a 10 mW 632.8 nm helium−neon laser, using noninvasive backscatter with a scattering angle of 173° and the temperature at 25 °C. Transmission electron microscopy (TEM) samples were prepared by suspending the dried nanoparticles in distilled water and then casting on Formvar TEM grids (Ted Pella Inc.). TEM images were obtained with a JEOL 1200EX TEM operated at 60 kV and a JEOL 1400 Plus (XR 80 Camera) TEM operated at HV = 120 kV. Thermal analysis (DSC/TGA) was conducted using a TA Instruments (New Castle, DE) SDT Q600 dual DSC TGA using capped alumina pans. The temperature was ramped from 25-600 °C at a rate of 10 °C/min with a constant flow of air at a rate of 50 mL/min.

3. RESULTS AND DISCUSSION

$Pb(NO_3)_2$ and carbonate-containing solutions were combined to produce a precipitate of NPs. To control and limit particle growth, the capping agent tetraethylene glycol (TEG) was used to arrest the precipitation reactions and limit particles to the nanoscale. Incorporation of TEG also increases the viscosity of the reaction medium which helps slow the nanoparticle crystal growth. The polyol capping method is a well-established and reliable method for controlling the growth of nascent nanoparticles of both elements and compounds.[22−25] In our system, the capping agent binds to surface cations and stabilizes the surface to prevent further agglomeration. TEG specifically provides an optimal balance between nanoparticle surface coverage and solution viscosity. Our previous work with the arrested precipitation of barium sulfate nanoparticles demonstrated TEG's superiority in this respect over comparable known capping agents such as ethylene glycol, and poly(ethylene glycol).[12] Additionally, high-intensity sonication was applied to prevent particle aggregation during the synthesis.[19] In this current work we also incorporated microwave irradiation as an alternative energy source to ultrasonication. Curiously, only one reactant combination produced a significant difference in nanoparticle phase distribution.

PXRD analysis was used to identify the crystalline $PbCO_3$-containing phases through identification using the ICDD database. Scherrer peak-width-at-half-height analysis was used to determine the average TEG-capped NP diffracting nanocrystallite size. The results of 3 replicates for the 5 reactions are listed in Table 2. There are four crystal forms produced in this work: cerussite, $Pb(CO_3)$; hydrocerussite, $Pb_3(CO_3)_2(OH)_2$; abellaite, $NaPb_2(CO_3)_2(OH)$; the potassium analog of abellaite, $KPb_2(CO_3)_2(OH)$. There in fact are multiple known lead(II) carbonate phases with cerussite and hydrocerussite being the most common. Cerussite NPs (CNPs) have been previously reported.[14] A hydrocerussite nanophase has been reported but these were 2D materials with 2 dimensions on the micron scale.[26] The abellaite phase is much less common in general. The X-ray diffraction pattern for the abellaite phase was first observed in 1983.[27] The structure of abellaite was correctly characterized as $NaPb_2(CO_3)_2(OH)$ in 2002.[28] Its existence in nature was first reported in 2017.[29] For abellaite, no nanoparticle phases have previously been reported. Similarly the potassium analog of abellaite has been structurally characterized[30] but there are no corresponding reports of nanoscale phases.

Reaction with Na_2CO_3 produces abellaite nanoparticles (ANPs) almost exclusively (>99% averaged over three syntheses) irrespective of whether energization occurs ultrasonically or by microwave irradiation (Figure 2). Additionally, Scherrer size analysis determined no statistical difference in nanocrystallite diameters (21−22 nm) for the two procedures.

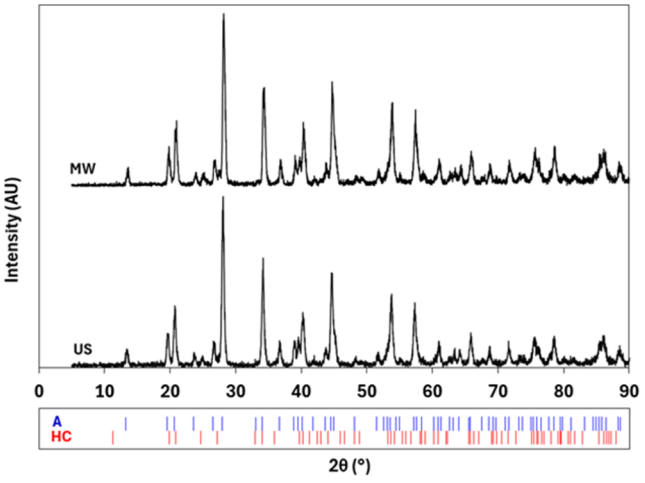

Figure 2. PXRD patterns measured for the Na_2CO_3 reaction products using ultrasonication (**US**) or microwave irradiation (**MW**). Abellaite (**A**, ICDD #01-086-9762) and hydrocerussite (**HC**, ICDD #01-088-6821) phases were identified.

https://doi.org/10.1021/acsomega.4c08839
ACS Omega 2024, 9, 48802−48809

Small quantities of hydrocerussite nanoparticles (HCNPs) are evident from the two strongest reflections of this phase at 2θ values not significantly overlapping with those of abellaite (24.9 and 49.8°) but these are insufficient for reliable size determination of HCNPs.

A more significant difference in outcome occurs with the synthesis using K_2CO_3. Energization of the precipitating solution using ultrasonication produces almost exclusively hydrocerussite nanoparticles (HCNPs) that were 25 nm in diameter. A trace quantity of the potassium analog of abellaite, $KPb_2(CO_3)_2(OH)$ (KPbNPs), was detected. However, using microwave irradiation, a mixed-phase nanoparticle system was produced with both KPbNPs and HCNPs significantly present in a 3:2 ratio as determined by WPPF/RIR analysis of the PXRD pattern (Figure 3). The nanocrystallite dimensions of

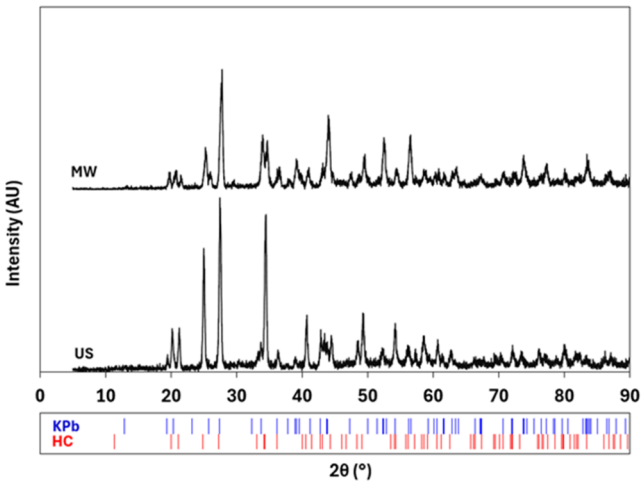

Figure 3. PXRD patterns measured for the K_2CO_3 reaction products using ultrasonication (**US**) or microwave irradiation (**MW**). $KPb_2(CO_3)_2(OH)$ (**KPb**, ICDD #01-086-6482) and hydrocerussite (**HC**, ICDD #01-088-6821) phases were identified.

both phases were determined to be about the same (21 and 23 nm, respectively). The difference in product distribution between US and microwave irradiation may be due to difference in energy input and dispersal. Ultrasound deposits energy in a less uniform manner with local hot spots caused by cavitation that can result in very high local temperatures. This type of input should favor the formation of kinetically favored products. Microwave irradiation will provide more uniform energy with few hot spots. This system should favor thermodynamically favored products. This suggests the KPbNPs are thermodynamically favored relative to the HCNPs.

Reactions with $(NH_4)_2CO_3$, NH_4HCO_3, and $NaHCO_3$ produce exclusively cerussite nanoparticles (CNPs), all in the range of 19−25 nm in size and irrespective of energization method. PXRD patterns are shown in Figures S1−S6.

The infrared spectra of the products resulting from the reactions using Na_2CO_3 and K_2CO_3 are presented in Figure 4 and have been cross-checked with FTIR spectra previously reported for bulk samples.[27] Common to all three identified phases of ANPs, KPbNPs, and HCNPs, are the υ_2 (842 cm^{-1}), υ_1 (1048 cm^{-1}), $\upsilon_1 + \upsilon_4$ (1740 cm^{-1}), and the especially prominent υ_3 (1400 cm^{-1}) CO_3^{2-} stretching modes. ANPs produced by either ultrasonication or microwave irradiation show identical FTIR spectra, unique to which is the strong

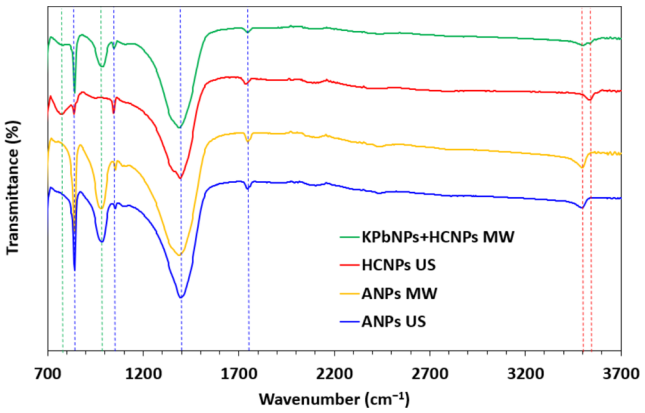

Figure 4. ATR-FTIR spectra for the NP samples: products from ultrasonicated (**US**) reactions with Na_2CO_3 (solid blue) and K_2CO_3 (solid red); products from microwave irradiated (**MW**) reactions with Na_2CO_3 (solid yellow) and K_2CO_3 (solid green); $\upsilon_{CO_3^{2-}}$ stretching modes (dashed blue); δ_{PbOH} bending modes (dashed green); υ_{OH} stretching modes (dashed red).

δ_{PbOH} bending mode at 984 cm^{-1}, while the corresponding much weaker deformation for hydrocerussite appears at 775 cm^{-1}. A distinctive feature observed in the spectra of ANPs and HCNPs is the presence of a single sharp, weak υ_{OH} stretching band at 3500 and 3540 cm^{-1}, respectively, indicating the presence of the hydroxyl groups, which are conspicuously absent from that of the CNPs (Figure S7−S9). The sharpness of these υ_{OH} absorptions and the lack of any other broad resonances in this region of the FTIR spectra indicate that there is little or no retention of water in either of these phases. Confirmation that both KPbNPs and HCNPs are produced together in the microwave-driven reaction with K_2CO_3 can be seen in the FTIR spectrum in Figure 4. Specifically, two distinct δ_{PbOH} resonances at 775 cm^{-1} (HCNPs) and 985 cm^{-1} (KPbNPs) and two υ_{OH} resonances at 3500 cm^{-1} (KPbNPs) and 3540 cm^{-1} (HCNPs) are observed. Interestingly, there is no evidence of the presence of TEG in any of the FTIR spectra, which should show its most intense resonances at ca. 1100 (υ_{CO}), 2900 (υ_{CH}), and 3400 cm^{-1} (υ_{OH}). This suggests that while TEG plays a critical role in the formation and size-control of the nanoparticles, it does not ultimately bind strongly to the surface and must easily be washed away during workup procedures. Perhaps, therefore, TEG functions more importantly as a viscosity control agent rather than as a capping agent during precipitation.

The reactions to produce each of the four crystal phases are shown in eqs 2−4. HCO_3^- is the reactant for eq 3 as this is the predominant form of the ion at the pH for the ammonium carbonates and sodium bicarbonate solutions. For eqs 2 and 4 the reactant is listed as CO_3^{2-} as this is the predominant form of carbonate at the pH of the metal carbonate solutions. The calculated pH values for the five reactants are shown above in Table 1. While the overall pH of the bulk solution does not reach these values, the local volume where nanocrystals are forming will have pH values in this range for the diffusion-controlled process. For comparison, we carried out the precipitation reaction of sodium carbonate with $Pb(NO_3)_2$ in pure water (no TEG) without energization. We observe the formation of a mixed-phase product consisting of cerussite and abellaite. The formation of hydrocerussite, a hydroxide-containing phase, is known to be preferred over that of

https://doi.org/10.1021/acsomega.4c08839
ACS Omega 2024, 9, 48802−48809

cerussite in water at higher temperatures.[31] Previous reports on abellaite have utilized hydrothermal synthesis methods.[28] These results are consistent with the preferred formation of abellaite, also a hydroxide-containing phase, with energy input from sonication. We observe ANPs, KPbNPs, and HCNPs formation with the more alkaline reactants. This is consistent with the need for OH^- reactant for these phases. The more neutral reactants, ammonium carbonate and sodium bicarbonate, produce CNPs. Thus, the presence of hydroxide in the solution drives the products through pathways **2** and **4**. Because of the novelty of the nanoparticles produced from the reactions with the Group 1 metal carbonates, only they are henceforth discussed.

$$2Pb(NO_3)_2(aq) + M^+(aq) + 2CO_3^{2-}(aq) + OH^-(aq) \rightarrow MPb_2(CO_3)_2(OH)(s) + 4NO_3^-(aq)\ (M^+ = Na^+ \text{or } K^+) \quad (2)$$

$$Pb(NO_3)_2(aq) + HCO_3^-(aq) \rightarrow PbCO_3(s) + 2NO_3^-(aq) + H^+(aq) \quad (3)$$

$$3Pb(NO_3)_2(aq) + 2CO_3^{2-}(aq) + 2OH^-(aq) \rightarrow Pb_3(CO_3)_2(OH)_2(s) + 6NO_3^-(aq) \quad (4)$$

The sizes, shape, and morphologies of the ANPs were visualized using TEM (Figure 5). The NPs were mostly

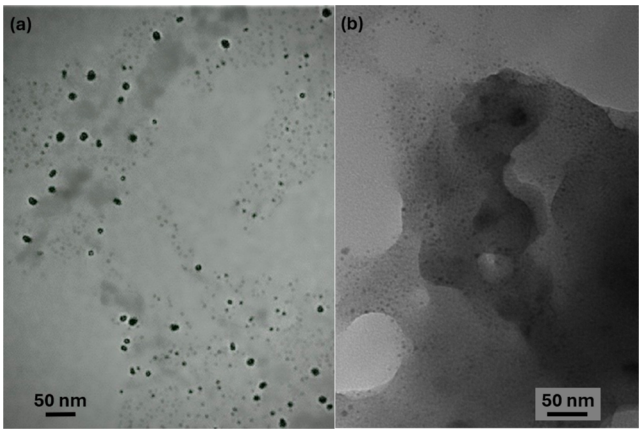

Figure 5. TEM images of (a) ANPs produced by ultrasonication and (b) ANPs produced by microwave irradiation.

spherical in shape, with some agglomeration observed being most likely due to the TEM grid preparation method. ANPs produced by ultrasonication are shown in Figure 5a. The array is dominated by more obvious larger particles that are in the range 10−30 nm. However, closer inspection shows that there appear to be many particles <10 nm in diameter, and some even down to 5 nm. This is even more apparent in the corresponding image for the ANPs produced by microwave energization in Figure 5b. There are some particles in the 20−30 nm diameter range but a great many more that are ca. 5−10 nm, suggesting a loosely bimodal distribution. While this might seem inconsistent with PXRD analyses, which indicated particle sizes just above 20 nm for both nanomaterials, PXRD peaks will have widths that reflect the larger nanoparticles, masking the broader and weaker peaks arising from the much smaller ones. Thus, only TEM can reveal the smallest of nanoparticles in these products. Even if the number-average of particles <10 nm is greater than those that are >20 nm, the mass-volume average will dictate the PXRD peak widths and this suggests that by mass, those larger nanoparticles dominate our samples.

TEM analysis of the products from the reaction using K_2CO_3 are shown in Figure 6. The product produced by

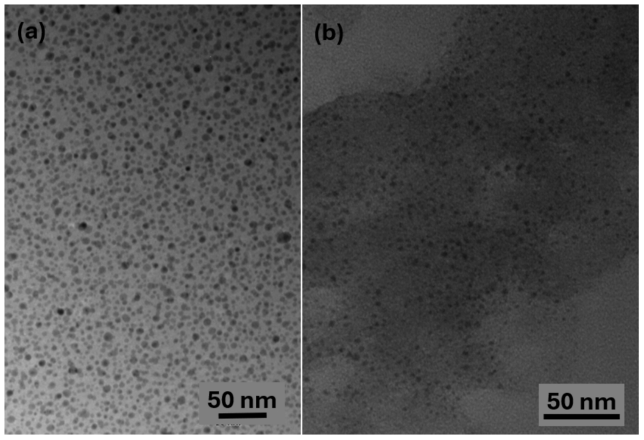

Figure 6. TEM images of (a) HCNPs produced by ultrasonication and (b) KPbNPs and HCNPs produced by microwave irradiation.

ultrasonication (Figure 6a) is almost entirely composed of HCNPs. As with the ANPs, they are spherical in morphology. The largest particles are in the 15−25 nm range in agreement with PXRD results, but again, there are clearly many much smaller particles that are <10 nm in diameter. This is the first observation of zero dimensional HCNPs. The product produced by microwave irradiation (Figure 6b) is a mixture of KPbNPs and HCNPs in a 3:2 mass ratio. Despite this, the micrograph shows a somewhat uniform collection of spheroidal nanoparticles, many of which are again <10 nm in diameter, reflecting size polydispersity, although individual nanoparticles >20−30 nm in size were observed.

More detailed DLS analysis permits judgment regarding the colloidal dispersibility and homogeneity of lead salt nanoparticles, something that is important for potential vascular micro-CT perfusion and imaging applications with these nanoparticles. Nanoparticles that aggregate quickly and easily fall out of suspension will resist uniform transportation through capillaries and be more likely to rupture blood vessels during perfusion. The DLS size plots for nanoparticles dispersed in liquid TEG are shown in Figure 7. DLS sizing analysis revealed that NP colloidal dispersions were well-dispersed and homogeneous with monomodal size distributions. ANPs, whether synthesized from Na_2CO_3 and $Pb(NO_3)_2$ using ultrasonication or microwave irradiation, formed agglomerates averaging ca. 825 nm in size, with microwaved nanoparticles showing a slightly narrower size distribution. HCNPs synthesized from K_2CO_3 and $Pb(NO_3)_2$ using ultrasonication formed agglomerates that were ca. 715 nm on average. The nanoparticle agglomerates of KPbNPs with HCNPs produced by microwave irradiation were slightly smaller at 615 nm. Their size distribution is comparably monomodal, however, which suggests that either KPbNPs and HCNPs are agglomerating together relatively homogeneously, or distinct phase agglomerates are coincidentally similar in size and polydispersity. Small salt-based nanoparticles with their high surface areas will

https://doi.org/10.1021/acsomega.4c08839
ACS Omega 2024, 9, 48802−48809

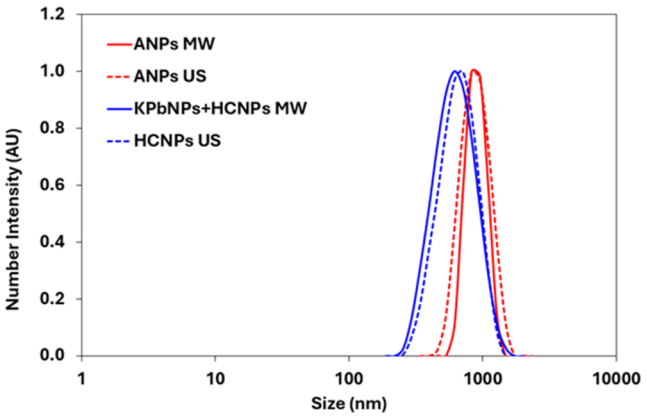

Figure 7. DLS size plots showing results averaged from 3 separate measurements of each sample dispersed in TEG: products (ANPs) from reaction using Na_2CO_3 (blue); products (KPbNPs + HCNPs or HCNPs) from reaction using K_2CO_3 (red); products formed using ultrasonication (**US**) (dashed); products formed using microwave irradiation (**MW**) (solid).

tend to agglomerate to some extent, even in polar media such as TEG because van der Waals attractive forces (resulting especially from large Pb^{2+} cations) cannot be completely overcome by electrostatic surface repulsions between nanoparticles. Surface modifications that can enhance electrostatic repulsions and mitigate agglomeration with these specific systems are currently under investigation.

A DSC/TGA scan for the ANPs is presented in Figure 8. For ANPs synthesized using ultrasonication, a 13.2% weight

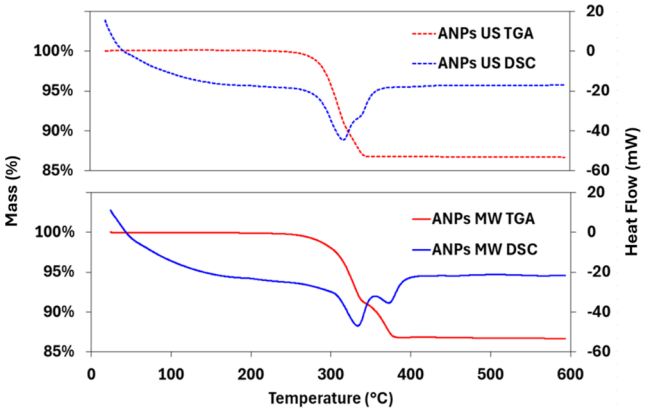

Figure 8. DSC (blue) and TGA (red) curves for ANPs (heating rate = 10 °C/min); product formed using ultrasonication (**US**) (dashed); product formed using microwave irradiation (**MW**) (solid).

loss is observed to occur in the range 300−350 °C. This appears to be a 2-stage decomposition that is more clearly observed from the DSC curve, with a principal endotherm at 315 °C and a shoulder at 340 °C. Exactly the same 13.2% weight loss is observed for the product isolated following microwave energization, although the two-stage decomposition process is even more apparent with now 2 distinct endotherms at 330 and 375 °C.

$$2NaPb_2(CO_3)_2(OH)(s) \rightarrow Na_2CO_3(s) + 2Pb_2O(CO_3)(s) + CO_2(g) + H_2O(g) \quad (5)$$

$$Pb_2O(CO_3)(s) \rightarrow 2PbO(s) + CO_2(g) \quad (6)$$

$$2NaPb_2(CO_3)_2(OH)(s) \rightarrow Na_2CO_3(s) + 4PbO(s) + 3CO_2(g) + H_2O(g) \quad (7)$$

The calculated combined weight loss for this pathway is 13.1%, which very closely matches that measured. The small discrepancy is most likely attributed to the presence of very small amounts HCNPs or possibly microscopic quantities of residual TEG or water, although no FTIR spectroscopic signatures were observed for either. In support of this, PXRD analysis of both thermalized products was shown to be the same: a mixture of PbO (massicot) and Na_2CO_3 (natrite) (Figures S10 and S11).

The DSC/TGA scans for the products produced from the reaction with K_2CO_3 are slightly more complex in nature (Figure 9). The product produced by ultrasonication is almost

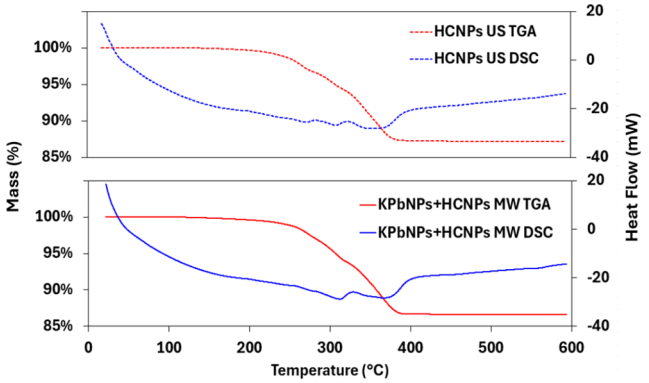

Figure 9. DSC (blue) and TGA (red) curves for HCNPs and KPbNPs + HCNPs (heating rate = 10 °C/min); product formed using ultrasonication (**US**) (dashed); product formed using microwave irradiation (**MW**) (solid).

entirely composed of HCNPs. The thermal decomposition of bulk hydrocerussite has been reported to occur in a more complex series of steps than originally reported.[32] This is also apparent for the nanoscale phase from the TGA curve in Figure 9, with at least 3 weight loss stages discernible between 200 and 380 °C along with poorly separated endotherms at 275, 310, and 360 °C in the DSC curve, the latter clearly broad and likely the result of two inseparable endothermic events. The overall process is nevertheless straightforward according to eq 8, with decomposition through the intermediacy of $Pb_3O(CO_3)_2$ first (due to water loss) and then $Pb_3(CO_2)O_2$, and possibly even $Pb_7O_3(CO_3)_4$ (due to progressive carbonate breakdown). This was supported by the observation of PbO (massicot) only in the PXRD analysis of the thermalized product (Figure S12).

$$Pb_3(CO_3)_2(OH)_2(s) \rightarrow 3PbO(s) + CO_2(g) + H_2O(g) \quad (8)$$

The TGA curve indicates a 12.8% weight loss in the range 200−375 °C, which is actually lower than the 13.6% expected total weight loss for the given mass of HCNPs. The most reasonable explanation for this would be the presence of some KPbNPs, which could be up to 5 wt % according to WPPF/RIR analysis in the PXRD measurements of several batches. Thus, residual potassium carbonate formed by the decom-

https://doi.org/10.1021/acsomega.4c08839
ACS Omega 2024, 9, 48802−48809

position of the KPbNPs (eq 9)[30] will reduce the % weight loss from that calculated for pure HCNPs.

$$2KPb_2(CO_3)_2(OH)(s) \rightarrow K_2CO_3(s) + 4PbO(s) + 3CO_2(g) + H_2O(g) \quad (9)$$

DSC/TGA curves for the mixed-phase product produced by microwave irradiation are comparably complicated. This is not surprising given the observation of overlapping endothermic decomposition processes in the 200−380 °C temperature range. The measured overall weight loss of 13.4% from the TGA curve is reasonably close, however, to that calculated (13.1%) for a sample composed of 3:2 KPbNPs/HCNPs by mass. Only peaks for PbO (massicot) could be confidently identified in post-DSC/TGA PXRD analysis, however (Figure S13). This is likely due to fortuitous masking of the strongest K_2CO_3 peaks by much more intense PbO peaks, because a thermalized sample of 3:2 KPbNPs/HCNPs should ultimately contain less than 15% K_2CO_3 by mass, and also due to poor signal-to-noise ratio.

4. CONCLUSIONS

We presented the first synthesis and observation of ANPs, KPbNPs, and of 0-D HCNPs. The syntheses were performed using high power ultrasound in TEG mixed with water or by using microwave irradiation, which was as effective at limiting crystallites to the nanoscale as sonication and is more amenable to further scale-up. Alkaline carbonate precursor solutions lead to production of the hydroxide-containing phases (ANPs, HCNPs) while the more acidic precursor carbonates lead to production of CNPs.

The hydroxide-containing nanophase products may be particularly useful in our vascular imaging application. The basic principle of our approach is to use alginate as a gelling agent for post-mortem micro-CT imaging as an alternative to standard histology. High X-ray contrast nanoparticles are entrained in the alginate solution upon perfusion. Following perfusion a divalent metal cation is included to cross-link the alginate to produce a stable gel for imaging. Previously, we used $BaSO_4$ nanoparticles as the contrast agent. However, $BaSO_4$ is not acid-reactive and cannot release Ba^{2+} for cross-linking. The current hydroxide-containing phases ANPs, HCNPs, and KPbNPs are all acid-reactive and can release Pb^{2+} for initial alginate cross-linking. Additionally, all these phases are more dense and have higher X-ray contrast than $BaSO_4$. This provides better contrast and requires lower NP concentrations in the perfusion solution which aids in accessing the fine vasculature by the final nanoparticle-alginate composite. Additionally, the hydroxide-containing phases may be particularly useful in formation of gels for vascular CT imaging as the divalent metal cations can be released with lower production of the CO_2 product which can reduce bubble formation within the gels. We will present future work on the gel-forming properties of these NPs and their application in vascular imaging.

■ ASSOCIATED CONTENT

Data Availability Statement

All underlying data available in the article itself and its Supporting Information.

Supporting Information

The Supporting Information is available free of charge at https://pubs.acs.org/doi/10.1021/acsomega.4c08839.

PXRD patterns (Figures S1−S6) and FTIR spectra (Figures S7−S9) for CNPs; PXRD patterns (Figures S10−S13) for post-DSC/TGA thermalized ANPs, HCNPs, and KPbNPs + HCNPs (PDF)

■ AUTHOR INFORMATION

Corresponding Authors

Steven W. Buckner − *Department of Chemistry, Saint Louis University, St. Louis, Missouri 63103, United States;* orcid.org/0000-0003-3630-0753; Email: steven.buckner@slu.edu

Paul A. Jelliss − *Department of Chemistry, Saint Louis University, St. Louis, Missouri 63103, United States;* orcid.org/0000-0002-7578-0350; Email: paul.jelliss@slu.edu

Authors

Madhushika E. Gamage − *Department of Chemistry, Saint Louis University, St. Louis, Missouri 63103, United States*

Kyan D. Ho − *Department of Chemistry, Saint Louis University, St. Louis, Missouri 63103, United States*

Mohammad S. Kader − *Department of Chemistry, Saint Louis University, St. Louis, Missouri 63103, United States*

Katherine Nguyen − *Department of Chemistry, Saint Louis University, St. Louis, Missouri 63103, United States*

Mirudhula Velmurugan − *Department of Chemistry, Saint Louis University, St. Louis, Missouri 63103, United States*

Sara H. McBride-Gagyi − *Department of Biomedical Engineering, The Ohio State University, Columbus, Ohio 43210, United States*

Complete contact information is available at: https://pubs.acs.org/10.1021/acsomega.4c08839

Author Contributions

The manuscript was written through contributions of all authors. All authors have given approval to the final version of the manuscript.

Funding

Saint Louis University School of Science & Engineering Competitive Research Grant.

Notes

The authors declare no competing financial interest.

■ ACKNOWLEDGMENTS

We thank Damon Osbourn, Ph.D., for assistance with instrumentation at SLU.

■ ABBREVIATIONS

CT, computed tomography; US, ultrasonic; MW, microwave; PXRD, powder X-ray diffraction; WPPF/RIR, whole powder pattern fitting/reference intensity ratio; ICDD, International Centre for Diffraction Data; ATR-FTIR, attenuated total reflectance − Fourier transform infrared; DLS, dynamic light scattering; TEM, transmission electron microscopy; DSC/TGA, differential scanning calorimetry/thermogravimetric analysis; TEG, tetraethylene glycol; ANPs, abellaite nanoparticles; KPbNPs, nanoparticles of the potassium analog of abellaite; HCNPs, hydrocerussite nanoparticles; CNPs, cerussite nanoparticles

REFERENCES

(1) Hubbell, J. H.; Seltzer, S. M. Tables of X-ray mass attenuation coefficients and mass energy-absorption coefficients 1 KeV to 20 MeV for elements Z = 1 to 92 and 48 additional substances of dosimetric interest. United States, 1995.

(2) Lusic, H.; Grinstaff, M. W. X-ray-computed tomography contrast agents. *Chem. Rev.* **2013**, *113* (3), 1641−1666.

(3) Buzug, T. M. Computed tomography. In *Springer Handbook of Medical Technology*; Springer, 2011; pp 311−342.

(4) Bui, T.; Stevenson, J.; Hoekman, J.; Zhang, S.; Maravilla, K.; Ho, R. J. Y. Novel Gd nanoparticles enhance vascular contrast for high-resolution magnetic resonance imaging. *PLoS One* **2010**, *5* (9), No. e13082.

(5) Vasquez, S. X.; Gao, F.; Su, F.; Grijalva, V.; Pope, J.; Martin, B.; Stinstra, J.; Masner, M.; Shah, N.; Weinstein, D. M.; Farias-Eisner, R.; Reddy, S. T. Optimization of MicroCT Imaging and Blood Vessel Diameter Quantitation of Preclinical Specimen Vasculature with Radiopaque Polymer Injection Medium. *PLoS One* **2011**, *6* (4), No. e19099.

(6) Kingston, M. J.; Perriman, D. M.; Neeman, T.; Smith, P. N.; Webb, A. L. Contrast agent comparison for three-dimensional micro-CT angiography: A cadaveric study. *Contrast Media Mol. Imaging* **2016**, *11* (4), 319−324.

(7) Koudrina, A.; O'Brien, J.; Garcia, R.; Boisjoli, S.; Kan, P. T. M.; Tsai, E. C.; DeRosa, M. C. Assessment of aptamer-targeted contrast agents for monitoring of blood clots in computed tomography and fluoroscopy imaging. *Bioconjugate Chem.* **2020**, *31* (12), 2737−2749.

(8) Lee, G. H.; Chang, Y.; Kim, T.-J. Synthesis and surface modification. In *Ultrasmall Lanthanide Oxide Nanoparticles for Biomedical Imaging and Therapy*; Lee, G. H.; Chang, Y.; Kim, T.-J., Eds.; 2014; pp 29−41.

(9) Rees, M. J. W.; Taylor, G. I. A simplified lead oxide cadaver injection technique. *Plast. Reconstr. Surg.* **1986**, *77* (1), 141−145.

(10) Al Saidi, A. K. A.; Baek, A.; Liu, S.; Mengesha, T. T.; Ahmad, M. Y.; Zhao, D.; Liu, Y.; Yang, J.-u.; Park, J. A.; Hwang, D. W.; Chae, K. S.; Nam, S.-W.; Chang, Y.; Lee, G. H. Lead oxide nanoparticles as X-ray contrast agents for in vitro and in vivo imaging. *ACS Appl. Nano Mater.* **2023**, *6* (21), 20129−20138.

(11) Bettini, A.; Patrick, P. S.; Day, R. M.; Stuckey, D. J. CT-visible microspheres enable whole-body in vivo tracking of injectable tissue engineering scaffolds. *Adv. Healthcare Mater.* **2024**, *13* (17), No. 2303588.

(12) Kader, M. S.; Weyer, C.; Avila, A.; Stealey, S.; Sell, S.; Zustiak, S. P.; Buckner, S.; McBride-Gagyi, S.; Jelliss, P. A. Synthesis and Characterization of $BaSO_4$-$CaCO_3$-alginate nanocomposite materials as contrast agents for fine vascular imaging. *ACS Mater. Au* **2022**, *2* (3), 260−268.

(13) McBride-Gagyi, S.; Buckner, S. W.; Jelliss, P. A.; Kader, M. S. Nanoparticle-alginate gels for X-ray imaging of the vasculature. US11,672,875. 2023.

(14) Devamani, R. H. P.; Vijitha, A. G. B. Morphology and thermal studies of lead carbonate nanoparticles. *Int. J. Eng. Sci. Innovative Technol.* **2016**, *5* (1), 62−65.

(15) Muthuselvi, C.; Anbuselvi, T.; Pandiarajan, S. Synthesis and characterization of lead (II) chloride and lead (II) carbonate nanoparticles. *Rev. Res.* **2016**, *5* (10), 1−13.

(16) Ji-Zhi, C.; Qing-Ze, J.; Zhou-Ling, T. Improvement of the method for nanometer $PbCO_3$ powders preparation. *Chin. J. Appl. Chem.* **2004**, *21* (9), 962−965.

(17) Li, Q. Preparation and characterization of $PbCO_3$ nanosized particles. *China Powder Sci. Technol.* **2005**, *11*, 1−13.

(18) Zhang, J.; Lang, P. R.; Pyckhout-Hintzen, W.; Dhont, J. K. G. Controllable synthesis and self-assembly of $PbCO_3$ nanorods in shape-dependent nonionic w/o microemulsions. *Soft Matter* **2013**, *9* (31), 7576−7582.

(19) Bang, J. H.; Suslick, K. S. Applications of ultrasound to the synthesis of nanostructured materials. *Adv. Mater.* **2010**, *22* (10), 1039−1059.

(20) Fernández-Barahona, I.; Muñoz-Hernando, M.; Herranz, F. Microwave-Driven Synthesis of Iron-Oxide Nanoparticles for Molecular Imaging. *Molecules* **2019**, *24* (7), 1224.

(21) Yao, Y.; Chen, F.; Nie, A.; Lacey, S. D.; Jacob, R. J.; Xu, S.; Huang, Z.; Fu, K.; Dai, J.; Salamanca-Riba, L.; Zachariah, M. R.; Shahbazian-Yassar, R.; Hu, L. In Situ High Temperature Synthesis of Single-Component Metallic Nanoparticles. *ACS Cent. Sci.* **2017**, *3* (4), 294−301.

(22) Fiévet, F.; Ammar-Merah, S.; Brayner, R.; Chau, F.; Giraud, M.; Mammeri, F.; Peron, J.; Piquemal, J. Y.; Sicard, L.; Viau, G. The polyol process: a unique method for easy access to metal nanoparticles with tailored sizes, shapes and compositions. *Chem. Soc. Rev.* **2018**, *47* (14), 5187−5233.

(23) Khulbe, R.; Kandpal, A.; Prasad, J.; Chandra, B.; Kandpal, N. D. Polyol synthesis of nanoparticles: A decade of advancements and insights. *Asian J. Chem.* **2023**, *35*, 2618−2630.

(24) Ammar, S.; Fiévet, F. Polyol synthesis: A versatile wet-chemistry route for the design and production of functional inorganic nanoparticles. *Nanomaterials* **2020**, *10* (6), 1217.

(25) Ruz, P.; Sudarsan, V. Polyol method for synthesis of nanomaterials. In *Handbook on Synthesis Strategies for Advanced Materials*, Indian Institute of Metals Series, Tyagi, A. K.; Ningthoujam, R. S., Eds.; Springer: Singapore, 2021.

(26) Shi, Y.; Ji, Y.; Long, J.; Liang, Y.; Liu, Y.; Yu, Y.; Xiao, J.; Zhang, B. Unveiling hydrocerussite as an electrochemically stable active phase for efficient carbon dioxide electroreduction to formate. *Nat. Commun.* **2020**, *11* (1), No. 3415.

(27) Brooker, M. H.; Sunder, S.; Taylor, P.; Lopata, V. Infrared and Raman spectra and X-ray diffraction studies of solid lead(II) carbonates. *Can. J. Chem.* **1983**, *61*, 494−502.

(28) Belokoneva, E. L.; Al'-Ama, A. G.; Dimitrova, O. V.; Kurazhkovskaya, V. S.; Stefanovich, S. Y. Synthesis and crystal structure of new carbonate $NaPb_2(CO_3)_2(OH)$. *Crystallogr. Rep.* **2002**, *47* (2), 217−222.

(29) Ibáñez-Insa, J.; Elvira, J. J.; Llovet, X.; Perez-Cano, J.; Oriols, N.; Busquets-Maso, M.; Hernandez, S. Abellaite, $NaPb_2(CO_3)_2(OH)$, a new supergene mineral from the Eureka mine, Lleida province, Catalonia, Spain. *Eur. J. Mineral.* **2017**, *29* (5), 915−922.

(30) Bette, S.; Eggert, G.; Fischer, A.; Dinnebier, R. E. Glass-induced lead corrosion of heritage objects: Structural characterization of $K(OH)\cdot 2PbCO_3$. *Inorg. Chem.* **2017**, *56* (10), 5762−5770.

(31) Carr, D. S. Lead Compounds. In *Ullmann's Encyclopedia of Industrial Chemistry*, 6th ed.; Ley, C., Ed.; Wiley-VCH, 2000.

(32) Ciomartan, D. A.; Clark, R. J. H.; McDonald, L. J.; Odlyha, M. Studies on the thermal decomposition of basic lead(II) carbonate by Fourier-transform Raman spectroscopy, X-ray diffraction and thermal analysis. *J. Chem. Soc., Dalton Trans.* **1996**, No. 18, 3639−3645.

https://doi.org/10.1021/acsomega.4c08839
ACS Omega 2024, 9, 48802−48809